

Dust extinction in HII region IC 5146

Roberto Pietro Infurna¹, Marco Bianchi¹, Marco Dallacàdidio¹

¹Università degli Studi di Milano-Bicocca, Milano, Italy

Accepted XXX. Received YYY; in original form ZZZ

ABSTRACT

IC 5146, also known as the Cocoon Nebula, is a Galactic HII region ionized by the single B0 V star BD +46°3474. This emission nebula is embedded within a larger molecular cloud, suggesting a significant presence of dust. We investigated dust extinction using three independent diagnostic methods. First, Balmer decrements provide a direct estimate of $E(B - V)$ by comparing the observed $H\alpha/H\beta$ surface brightness ratio with the standard intrinsic value of 2.86. Second, we analyzed GAIA BP/RP spectra of five stars within the nebula, including the central ionizing star, by fitting a blackbody model with extinction to determine dust absorption. Lastly, we examined the theoretical Strömgren radius for different dust fractions to infer dust constraints indirectly. Our results confirm the presence of dust within the HII region, though it is not uniformly distributed. Most of the nebula exhibits low extinction ($E(B - V) \lesssim 0.3$), with localized regions experiencing higher attenuation. The extinction inferred from stellar spectra favors the Calzetti extinction law over the Cardelli law. While the $E(B - V)$ values derived from stellar spectra and Balmer decrements are of the same order of magnitude, they do not show perfect agreement. The Strömgren radius analysis confirmed the presence of dust in the HII region; however, it did not provide a more precise constraint on the reddening.

Key words: HII region – dust extinction – Strömgren sphere

1 INTRODUCTION

Hot and massive O and B-type stars emit most of their radiation in the UV spectrum, which leads to the full ionization of surrounding gas. These regions, known as HII regions, often exhibit spherical symmetry, with the hot star in their center. They are characterized by strong emission lines due to recombination processes. In the context of Case B recombination (Osterbrock, 1989), when a hydrogen atom recombines with an electron and transitions to the $n = 1$ ground state, it emits a photon in the Lyman series (e.g., Lyman- α). However, in this regime, the Lyman photons are reabsorbed and reprocessed within the gas because the medium is optically thick to ultraviolet photons in the Lyman series, preventing them from escaping the nebula. On the other hand, transitions involving higher energy levels (with $n > 1$), such as $H\alpha$ emission from $n = 3 \rightarrow 2$ or $H\beta$ from $n = 4 \rightarrow 2$, are optically thin. These photons can escape the nebula without significant reabsorption, making the Balmer, Paschen, and other hydrogen emission lines prominent in the observed spectrum.

1.1 Dust Extinction

Dust particles in the interstellar medium (ISM) are known to absorb and scatter light from celestial sources. In regions with abundant dust, such as in newly-formed HII regions within giant molecular clouds, the nebula can become optically thick. In such cases, the emission we observe may only come from the outermost layers of the nebula.

Since dust extinction is highly selective with wavelength, being more severe toward higher-energy (blue-UV) photons, the ratio of the $H\alpha$ to $H\beta$ emission lines can give insights into the optical thickness of the region. Dust extinction is defined as $A_\lambda =$

$2.5 \log(F_{0,\lambda}/F_\lambda)$, where $F_{0,\lambda}$ and F_λ are the intrinsic and observed fluxes. The optical depth is simply $\tau_\lambda = A_\lambda/1.086$. Extinction is often expressed as function of the color excess (or reddening) $E(B - V) = (B - V)_{\text{observed}} - (B - V)_{\text{intrinsic}}$ and of the extinction curve $k(\lambda)$:

$$A_\lambda = k(\lambda) E(B - V) \quad (1)$$

Reddening is a measure of the column density of dust, while the extinction curve depends on the microphysics of dust absorption. This last is often parametrized by the total-to-selective extinction ratio $R_V = A_V/(A_B - A_V) = A_V/E(B - V)$. Typical values in the Milky Way are $R_V \sim 3.1$, but they can range between 2 and 6 depending on dust composition: silicate-rich dust produces a steep extinction curve at short wavelengths (low R_V), while carbonaceous dust typically produces a flatter curve (higher R_V). Also the environment plays a role: typically in the diffuse ISM dust is made of small grains, while in dense clouds larger grains dominate due to coagulation or icy mantles, leading to higher R_V . In star-forming regions (HII regions) high radiation fields can destroy small grains, increasing R_V .

The two more popular extinction laws are the the Cardelli, Clayton, and Mathis (CCM89) extinction law (Cardelli et al., 1989) and the Calzetti extinction law (Calzetti et al., 2000), Fig. 1. CCM89 was derived from observations of stars in different galactic environments, primarily focusing on the Milky Way galactic plane. It shows a bump in the UV caused by the absorption features of carbonaceous dust grains, specifically polycyclic aromatic hydrocarbons (PAHs) and small graphite particles. Calzetti law is specifically designed to describe the dust extinction in starburst galaxies, and shows a steeper rise in extinction at shorter wavelengths (UV) compared to the CCM89 law. It lacks the UV bump.

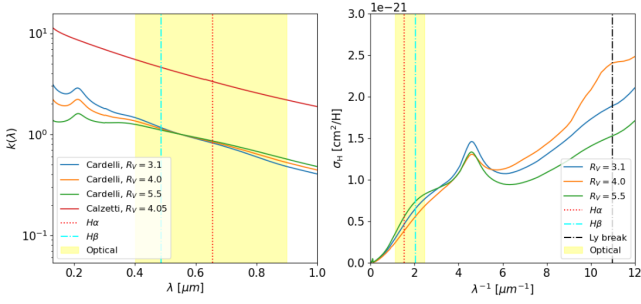


Figure 1. Adopted dust extinction curves per hydrogen atom. Left: $k(\lambda)$ for Calzetti (2000) and Cardelli (1989). Right: Dust absorption cross section per hydrogen atom (assuming uniform $n_{\text{dust}}/n_{\text{H}}$) for Cardelli, for different values of R_V .

Balmer decrement follows from the definition of reddening (Domínguez et al., 2013):

$$E(B - V) = \frac{2.5}{k(\lambda_{\text{H}\beta}) - k(\lambda_{\text{H}\alpha})} \log \left[\frac{(\text{H}\alpha/\text{H}\beta)_{\text{obs}}}{2.86} \right] \quad (2)$$

where $k(\lambda_{\text{H}\beta})$ and $k(\lambda_{\text{H}\alpha})$ are the extinction curves evaluated at $\text{H}\beta$ and $\text{H}\alpha$ wavelengths, respectively, assuming Calzetti law. The factor $E(\text{H}\beta - \text{H}\alpha)$ is analogous to the color excess but defined for $\text{H}\beta$ and $\text{H}\alpha$ instead of the B and V bands. $(\text{H}\alpha/\text{H}\beta)_{\text{int}}$ is the intrinsic or unreddened Balmer decrement, which at a temperature $T = 10^4$ K and electron density $n_e = 10^2 \text{ cm}^{-3}$ is 2.86 for Case B recombination (Osterbrock 1989). Therefore the ratio of the measured $\text{H}\alpha$ and $\text{H}\beta$ surface brightness is a diagnostic for the amount of dust present in the nebula.

1.2 Dusty Strömgren Sphere

In 1937, Bengt Strömgren developed a simple model to describe the size and ionization profile of HII regions. The model is based on the equilibrium between the number of ionizing photons emitted by the central star and the rate of hydrogen recombination within the region.

If we approximate the central star intrinsic spectrum to that of a perfect spherical black body of surface temperature T_* and radius R_* , the number of ionizing photons ($h\nu > 13.6$ eV) emitted per second is:

$$S_* = 4\pi R_*^2 \int_0^{91.2} \frac{B(T_*, \lambda)}{hc/\lambda} d\lambda \quad (3)$$

The transition from $x = 1$ (fully ionized) to $x = 0$ (fully neutral) is very steep (Fig. 2). We can approximate the ionization profile with a step function and define the Strömgren radius as the radius where hydrogen transitions from fully ionized to fully neutral. This occurs when the number of ionizing photons decreases to zero, as they are all been absorbed to balance hydrogen recombinations:

$$S_* = \int_0^{R_S} \alpha_B n_{\text{H}}^2 4\pi r^2 dr \quad (4)$$

where α_B is Case B recombination coefficient (Osterbrock, 1989). Assuming a uniform hydrogen density n_{H} and $x = 1$, this simplifies to:

$$R_S = \left(\frac{3S_*}{4\pi\alpha_B n_{\text{H}}^2} \right)^{1/3} \quad (5)$$

For typical gas number density of $n_{\text{H}} = 10^2 \text{ cm}^{-3}$ and O-B type central star the size of the HII region is of the order of ~ 1 parsec.

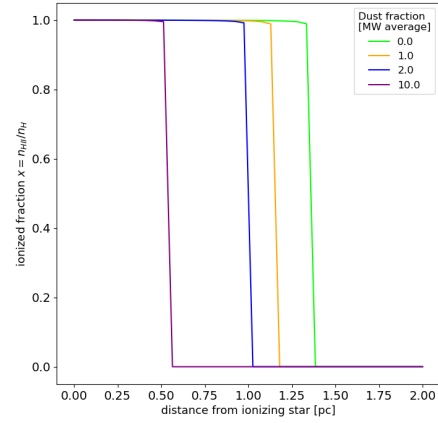


Figure 2. Self-consistent ionization profile for different $n_{\text{dust}}/n_{\text{H}}$ values, expressed in terms of the average ISM dust-to-gas mixing ratio (Draine, 2003). The profiles are obtained by solving $S_*/(4\pi r^2) \cdot e^{-\tau(r)} \cdot \sigma_{\text{H}}(1 - x) = x^2 n_{\text{H}} \alpha_B$, with S_* evaluated for $T_{\text{eff}} = 32000$ K and $R_* = 5.2R_{\odot}$ and $\sigma_{\text{H}} = 6.3 \times 10^{-18} \text{ cm}^2$. Optical depth is: $\tau(r) = \int_0^r [(1 - x(r')) \sigma_{\text{H}} n_{\text{H}} + \bar{\sigma}_{d, \text{H}} n_{\text{dust}}] dr'$. The profile is solved recursively, initializing $x(r) = 1$ everywhere and updating it at each step. The transition from $x = 1$ to 0 is steep, supporting the Strömgren assumption. Dust significantly influences the radius.

It is straightforward to correct for dust: dust grains reduce the number of ionizing photons by absorbing a fraction of the radiation. This introduces an additional term in the balance equation:

$$S_* = \int_0^{R_S} \beta_2 n_{\text{p}}^2 4\pi r^2 dr + \int_0^{R_S} \Gamma_{\text{dust}}(r) n_{\text{dust}} 4\pi r^2 dr \quad (6)$$

where $\Gamma_{\text{dust}}(r)$ is the rate of absorption by dust that depends on the flux of ionizing photons and on the dust effective cross section (averaged dust cross section per hydrogen atom for $\lambda < \text{Lyman break}$): $\Gamma_{\text{dust}}(r) = \frac{S_*}{4\pi r^2} e^{-\bar{\sigma}_{d, \text{H}} n_{\text{H}} r}$. Integrating:

$$S_* = \beta_2 n_{\text{H}}^2 \frac{4\pi}{3} R_S^3 + S_* \left(1 - e^{-\bar{\sigma}_{d, \text{H}} n_{\text{H}} R_S} \right) \quad (7)$$

The ultimate effect of dust is to reduce the number of ionizing photons of a factor $e^{-\tau_d}$. In terms of the reddening $E(B - V)$ and of the effective \bar{k} (averaged extinction curve for $\lambda < \text{Lyman break}$):

$$R_S = \left(\frac{3S_* e^{-\bar{k} E(B - V)/1.086}}{4\pi\alpha_B n_{\text{H}}^2} \right)^{1/3} \quad (8)$$

If the central star is well known, and the geometry is sufficiently easy, a measurement of the nebular projected radius can be compared to theoretical Strömgren radius to extract informations on the amount of dust mixed with the gas.

2 OBSERVATIONS

A total of five frames were acquired: one exposure of 900 s with the narrow $\text{H}\alpha$ filter on 28-10-2024 under optimal atmospheric conditions at the Milan site, and four exposures of 1200 s each with the narrow $\text{H}\beta$ filter on 30-10-2024, when the atmospheric conditions were slightly less favorable. The exposure time ensures a low signal-to-noise ratio ($\text{SNR} < 1$, for an estimated nebular surface brightness in $\text{H}\alpha$ of $\sim 10^{-14} \text{ erg s}^{-1} \text{ cm}^{-2} \text{ arcsec}^{-2}$). The SNR can be improved by applying filtering techniques. By averaging the signal over approximately 10–100 pixels, the SNR increases to $\gtrsim 5$.

2.1 Data Reduction

The initial steps of data reduction are the same for both the single $H\alpha$ frame and the four $H\beta$ frames.

The object frames were first converted from ADUs (Analog-to-Digital Units) to electrons by applying the TOBI gain factor of 0.6. Master dark frames were obtained by stacking three dark exposures of 900 s and three of 1200 s and computing the median. Dark frames include bias level and dark current. To correct for pixel sensitivity variations, five flat-field frames were taken for each filter on the same nights as the observations. These flats were stacked, averaged, and normalized to unity before application. The sky frame was obtained from:

$$\text{Sky Frame} = [\text{Object Frame} - \text{Dark Frame}] / \text{Flat normalized} \quad (9)$$

Following this, sky background subtraction was performed using the `Background2D` class from `photutils`. To prevent contamination from sources such as stars and extended emission, bright sources were masked using segmentation and thresholding techniques. Given the presence of a faint, extended nebula, a circular mask was manually applied to exclude it from the background estimation. The background was computed using a median estimator over a grid of 50×50 pixel boxes. A median filter of 3×3 pixels was then applied to smooth the background map before interpolation using the `BkgZoomInterpolator` function with a bicubic spline. This last stage was essential to extrapolate the background in the masked nebular region.

In the $H\beta$ filter, an additional step was required to correct for dithering between the four different exposures before stacking them together. Dithering between the $H\alpha$ and $H\beta$ images was also ultimately removed.

2.2 Calibration

Field stars were identified using the `Astrometry.net` software. A transformation map between pixel coordinates (x, y) and celestial coordinates (ra, dec) was fitted, enabling cross-calibration with archival datasets.

The photometric calibration was performed using XP spectra from the GAIA Data Release 3 (DR3). These spectra are low-resolution, prism-dispersed observations obtained with the BP/RP (Blue Photometer / Red Photometer) instruments onboard the GAIA space telescope. Field stars were selected within 0.15 arcmin from the central star (ra: 328.370 dec: +47.266) if magnitude in g band is < 13 . The specific flux in units of $\text{erg s}^{-1} \text{cm}^{-2} \text{\AA}^{-1}$ was computed by convolving each stellar spectrum with TOBI filter transmission curve, which accounts for both filter response and detector quantum efficiency (Q.E.):

$$f_{\lambda, \text{filter}} \approx \frac{\int d\lambda T(\lambda) f(\lambda)}{\int d\lambda T(\lambda)}. \quad (10)$$

The observed frames were divided by their respective exposure times to obtain measurements in electron/s. For each filter, the conversion factor to physical flux units is defined as:

$$f_{\lambda, \text{filter}} = 10^{-C} N_e, \quad (11)$$

where N_e is the measured electron rate on the detector, and $f_{\lambda, \text{filter}}$ is the specific flux derived from Eq. 10. Since each stellar point spread function (PSF) spans multiple pixels, the choice of photometric aperture was critical. An aperture of $1.2 \times \text{FWHM}$ was adopted, capturing $\geq 95\%$ of the encircled energy (EE) while minimizing contamination from the surrounding nebula. To determine the calibration factor

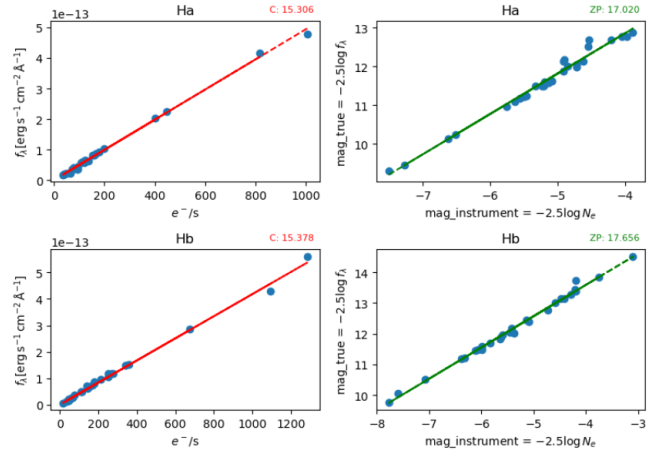


Figure 3. Determination of the conversion factor, 10^{-C} , between electrons s^{-1} per pixel and specific flux per pixel. A linear fit was performed on stellar photometry (measured using an aperture of $1.2 \times \text{FWHM}$) after convolving the GAIA BP/RP spectra with TOBI's filter transmission curves (see Equation 10). In the right panels, the specific flux and detector counts are converted to magnitudes via $-2.5 \log(f_{\lambda}) = 2.5C - 2.5 \log(N_e)$. An alternative calibration using SDSS data (with transformations between SDSS and TOBI responses) was also attempted, but it did not yield the same linearity.

C for each filter and to verify the linear response of the detector, a best-fit line was computed, as shown in Fig. 3.

Initially, an alternative calibration approach using the Sloan Digital Sky Survey (SDSS) dataset was tested. The SDSS archive provides magnitudes in the u, g, r, i, z bands for a significant number of field stars. These magnitudes were converted to the TOBI system using a set of linear transformations. However, the resulting calibration showed higher scatter compared to GAIA DR3. Consequently, GAIA DR3 spectra were preferred for the final calibration.

As a final step of the calibration, the measured values are multiplied by the effective widths of the $H\alpha$ and $H\beta$ filters (37.7\AA and 104.8\AA) and by the TOBI pixel scale ($1 \text{ pixel} = 0.44''$) to yield surface brightness in units of $\text{erg s}^{-1} \text{cm}^{-2} \text{arcsec}^{-2}$.

2.3 Noise Treatment

Instead of propagating Poissonian errors through each step of data reduction and calibration, we estimated the noise level at the final stage of the calibration process. The dominant noise sources are the bias level and the sky background. Subtracting these components does not remove fluctuations, so we analyzed the residual noise distribution to quantify its characteristics.

To estimate the noise, we examined the histogram of pixel values, which we expect to follow a Gaussian distribution centered around zero. Real sources appear as a positive tail, making the distribution asymmetric. To avoid contamination from real objects, we fitted a Gaussian to only the negative side of the histogram. This ensures that the error estimation is not biased by astronomical sources.

The first column of Fig. 4 presents the histogram of pixel values and the fitted Gaussian distributions for the $H\alpha$ and $H\beta$ observations. The measured noise level is $\sigma > 2 \times 10^{-15} \text{erg s}^{-1} \text{cm}^{-2} \text{arcsec}^{-2}$, corresponding to a signal-to-noise ratio below 1 in the faint regions of the nebula. To improve the SNR we filtered the image. Low-pass filters smooth the image by averaging pixel values within a local

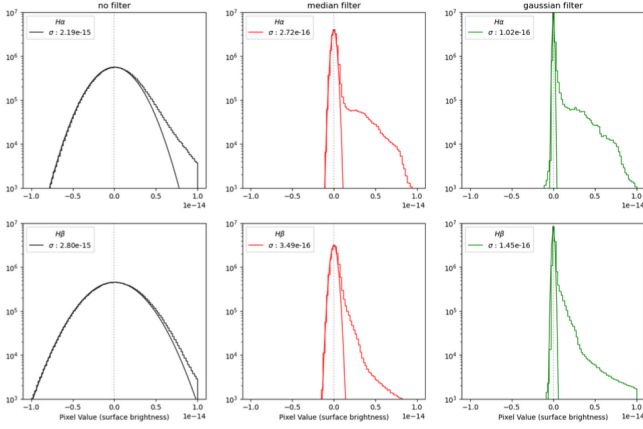


Figure 4. Effect of noise reduction on the initial image (left) using a median filter (center) and a Gaussian filter (right). The Gaussian, centered on zero, becomes narrower after filtering as the noise is averaged out, allowing the signal to emerge more clearly.

region, following the equation:

$$I'(x, y) = \sum_{u=-k}^k \sum_{v=-k}^k I(x+u, y+v) \cdot h(u, v) \quad (12)$$

where $h(u, v)$ represents the filter kernel, which defines the filter behavior, and k determines the kernel size. We tested two filters: median filter (replaces each pixel with the median of its local neighborhood), and Gaussian filter (applies a Gaussian-weighted smoothing). The level of blurring depends on the kernel size. We found that a Gaussian filter with $\sigma = 10$ or a median filter with a 10×10 kernel provides a good balance between improving *SNR* and maintaining image sharpness.

3 RESULTS

3.1 Balmer Decrement

After applying a low-pass filter to the image, we generated a map of $E(B - V)$ using Equation (2), as shown in Fig. 5. We are assuming Calzetti extinction law. Interestingly, most of the region does not exhibit a reddening parameter significantly different from the expected value of 2.86. Areas with high $E(B - V)$ coincide with dark regions in the $H\alpha$ and $H\beta$ surface brightness maps. However, it is likely that these high values are primarily due to the $H\beta$ flux approaching zero rather than actual reddening effects.

3.2 Stellar Spectra

We analyzed the GAIA BP/RP spectra of the central star and four other stars embedded in or located behind the nebula. While GAIA provides accurate distance measurements, it does not include surface temperature or radius estimates for these stars. For the central star, we adopted a surface temperature of $T_{\text{eff}} = 32,500$ K based on the work of Rojas et al. (2014), who analyzed high-resolution spectral signatures.

We fitted the spectra using a simple black body model with extinction, considering two different dust models: Calzetti ($R_V = 4.1$) and Cardelli ($R_V = 3.1$), Fig. 1. For the central star, we treated the stellar radius R_* and reddening $E(B - V)$ as free parameters. In contrast, for

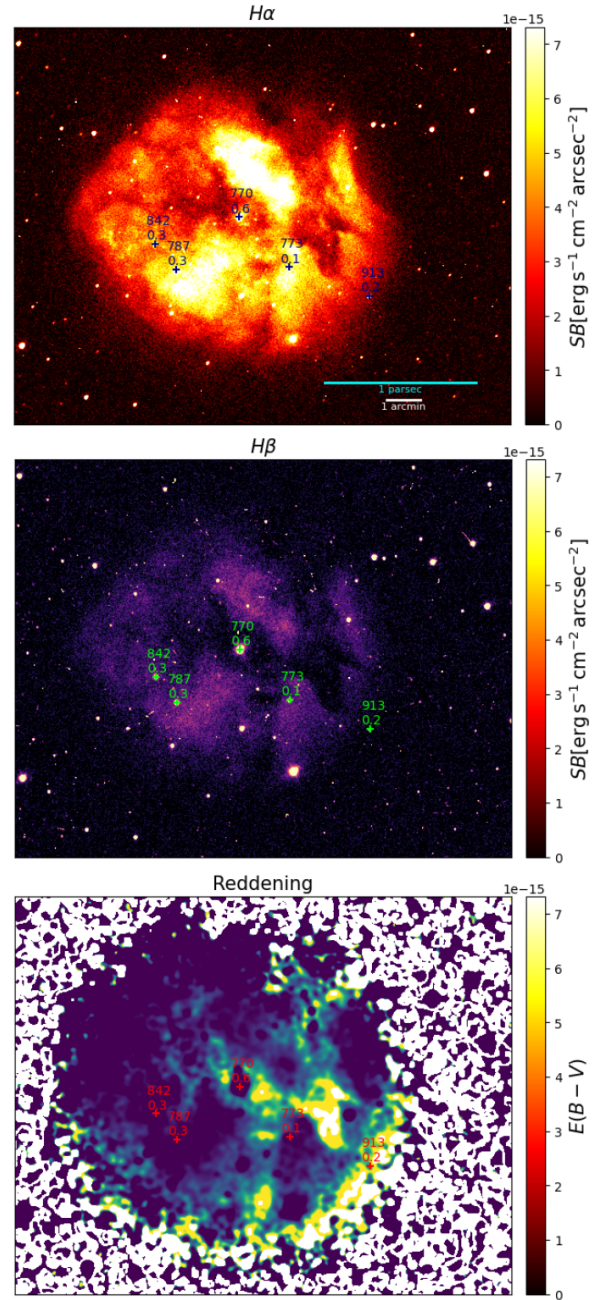


Figure 5. Surface brightness in $H\alpha$ and in $H\beta$ and reddening map of IC 5146. Overlaid on these maps are analyzed stars, with labels indicating their distance (in pc) and the reddening inferred from spectral fitting. To obtain the reddening map, $H\alpha$ and $H\beta$ images were smoothed using a Gaussian filter with $\sigma = 10$ pixels. The uncertainties after smoothing are $\sigma = 1.02 \times 10^{-16} \text{ erg s}^{-1} \text{ cm}^{-2} \text{ arcsec}^{-2}$ for $H\alpha$ and $\sigma = 1.45 \times 10^{-16} \text{ erg s}^{-1} \text{ cm}^{-2} \text{ arcsec}^{-2}$ for $H\beta$. Regions of high reddening are largely due to the $H\beta$ flux being indistinguishable from zero (with a Balmer decrement signal-to-noise ratio > 5) and are therefore not highly significant.

the other four stars, we had to treat the surface temperature T_{eff} as a free parameter as well. Spectra are presented in Fig. 6. The inferred reddening is highly sensitive to the choice of extinction curve.

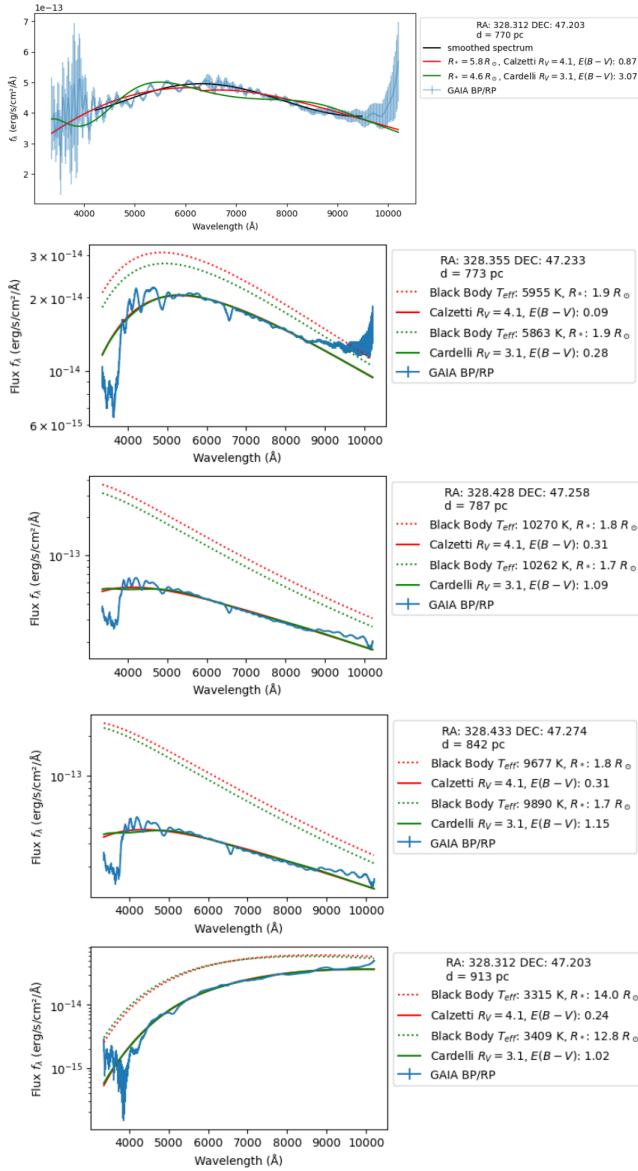


Figure 6. Spectra of stars embedded in the nebula, or behind it. First panel is the central star that ionizes the surrounding gas, BD +463474. The GAIA BP/RP spectrum exhibits artifacts, likely due to the star’s high luminosity, and therefore before fitting the spectrum with our model we smoothed the data (excluding wavelengths $\lambda < 4200 \text{ \AA}$ and $\lambda > 9500 \text{ \AA}$) using a fifth-order polynomial. The fitted model follows $(R_*/d)^2 \times \pi B_\lambda(T_{eff}) \times \exp[-k(\lambda)E(B-V)/1.086]$, where $d = 770 \text{ pc}$ is the distance, and $B_\lambda(T_{eff})$ represents the black body spectrum. The fit is strongly dependent on the choice of the dust extinction curve, with the Calzetti law yielding a much better result. To fit the other stars we used the same model but with three free parameters: R_* , T_{eff} , and $E(B-V)$. Potential degeneracies in the fitting process have not been explored. The same stars are marked in Fig. 5.

3.3 Strömgren Radius

Finally, we computed the Strömgren radius for the central star, assuming $T_{eff} = 32,500 \text{ K}$ and $R_* = 5.8 R_\odot$, along with typical HII region conditions of $n_H = 10^2 \text{ cm}^{-3}$ and $T_e = 10^4 \text{ K}$, while considering various values of $E(B-V)$. To assess the relative importance of dust absorption of ionizing photons, we compared the relevant cross sections. The effective dust cross section per hydrogen atom, $\tilde{\sigma}_{d,H}$, is es-

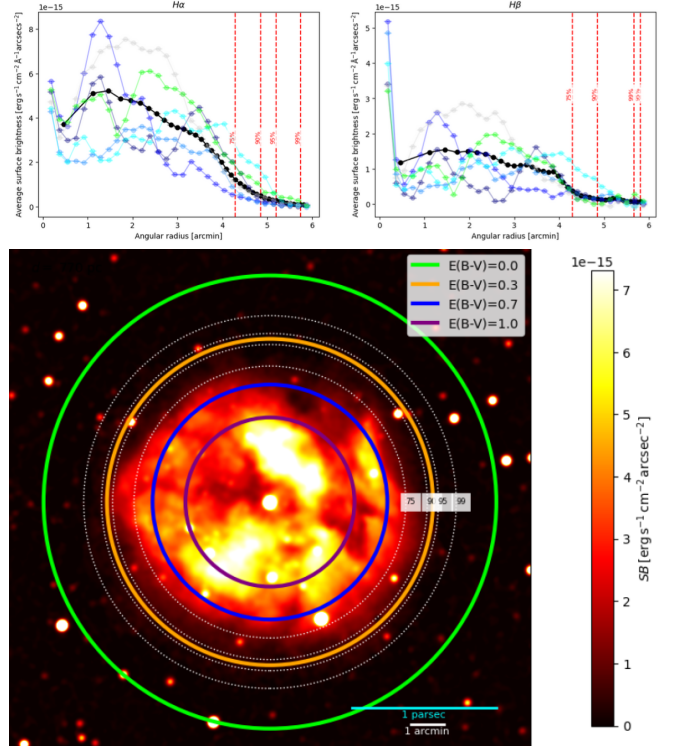


Figure 7. Top panels: Radial profiles of surface brightness in $H\alpha$ and $H\beta$, obtained by averaging along circular annuli (black curves) or sampling regions along different radial directions (colored curves). The 75%, 90%, 95%, and 99% isophotal radii are indicated. Bottom panel: A smoothed image of the nebula (processed with a Gaussian filter for visual clarity), overlaid with Strömgren radii corresponding to different dust reddening parameters. The same isophotal radii are shown for reference. Our analysis suggests that the average reddening is in the range 0.3-0.7, but no further precise constraints can be drawn.

timated to be $2.17 \times 10^{-21} \text{ cm}^2/\text{H}$, which is significantly smaller than the hydrogen photoionization cross section, $\sigma_H = 6.3 \times 10^{-18} \text{ cm}^2$.

We used the Fitzpatrick dust extinction curve with $R_V = 3.1$ (Draine, 2003) instead of the Calzetti law, as the latter is limited to the optical range. To analyze the nebula’s structure, we computed the surface brightness radial profile by averaging over circular annuli centered on the central star. Additionally, to account for possible anisotropies, we measured surface brightness along different radial directions. We then identified the radii at which the surface brightness drops by 75%, 90%, 95%, and 99%, Fig. 7.

The computed Strömgren radii for different values of $E(B-V)$ were overlaid onto the nebula, Fig. ?? The results suggest that values of reddening in the range 0.3-0.7 are most likely, consistent with both the Balmer decrement and stellar spectra fitting. Due to the model’s oversimplified assumptions—primarily the uniformity and symmetry of the region—more precise constraints on the dust amount cannot be determined.

4 CONCLUSIONS

Our investigation confirms the presence of dust in the HII region IC 5146, as expected, but fails to provide a precise constraint on the dust column density.

- The Balmer decrement method has been proposed to determine

reddening in galaxies (Domínguez et al., 2013). It assumes a uniform dust screen covering an underlying stellar population. However, this approach may not be as effective for self-emitting sources like HII regions, where each region simultaneously emits recombination lines and absorbs light due to dust. In such cases, the full radiative transfer equation must be solved:

$$I_{\lambda}(\tau_{\lambda}) = \int_0^{\tau_{\lambda}} e^{-(\tau_{\lambda}-\tau'_{\lambda})} S_{\lambda}(\tau'_{\lambda}) d\tau'_{\lambda} \quad (13)$$

Substituting the definition of dust optical depth, $\tau_{\lambda} = \sigma_{\lambda,H} n_H s$, and assuming a uniform n_H and emissivity j_{λ} , we obtain:

$$I_{\lambda}(s) = \frac{j_{\lambda}}{\sigma_{\lambda,H} n_H} (1 - e^{-\sigma_{\lambda,H} n_H s}) \quad (14)$$

where $s = 2R_{\text{cloud}} \sqrt{1 - (\frac{\theta}{\theta_{\text{cloud}}})^2}$ is a function of the projected angular radius. We attempted to compare the predicted surface brightness radial profile with observations but could not extract meaningful constraints. Several assumptions may fail, particularly those of uniform gas and dust distribution.

- The most robust indicators of dust extinction in our analysis come from stellar spectral fitting. However, potential degeneracies between reddening, surface temperature, and stellar radius cannot be excluded. All spectra suggest that the Calzetti dust law provides a better fit for extinction in this region than the Cardelli law and that the reddening remains below 1 across the nebula.

- The derived Strömgren radius is of the same order of magnitude as the surface brightness drop-off radius, confirming that IC 5146 is ionized by the central B0 V star BD +46°3474 rather than by multiple embedded stars. The presence of dust is also confirmed. However, the model relies on numerous assumptions, making it an unreliable diagnostic tool for dust fraction. It presumes precise knowledge of the central star parameters and assumes a well-mixed dust and gas distribution. An alternative scenario considers a central depletion region, where stellar winds have expelled gas and photodissociated molecules, a process observed in HII regions (McCullough, 2000). This would effectively enlarge the Strömgren radius, modifying the lower limit in integral (4). Consequently, any desired $E(B-V)$ value could be achieved by tuning this additional parameter. It is also important to note that for the Strömgren analysis, we had to compute an effective dust absorption cross-section for wavelengths shorter than the Lyman break. We adopted the Cardelli/Fitzpatrick dust law, as the cross-sections have been estimated in the UV range (Draine, 2003). In contrast, the Calzetti law, which better describes stellar spectra (Fig. 6), is limited to the optical and near-UV ranges.

REFERENCES

- Cardelli, J. A., Clayton, G. C., & Mathis, J. S. 1989, *ApJ*, 345, 245. <https://doi.org/10.1086/167900>
- Calzetti, D., Armus, L., Bohlin, R. C., et al. 2000, *ApJ*, 533, 682. <https://doi.org/10.1086/308692>
- Domínguez, M. A., Pérez, E., Ruiz, N., et al. 2013, *A&A*, 558, A48. <https://doi.org/10.1051/0004-6361/201322346>
- Draine, B. T. 2003, *ARA&A*, 41, 241. <https://doi.org/10.1146/annurev.astro.41.011802.094844>
- McCullough, P. R. 2000, *A&A*, 357, 231.
- Osterbrock, D. E. 1989, *Astrophysics of Gaseous Nebulae and Active Galactic Nuclei*, University Science Books.
- Rojas, A. L., Cid Fernandes, R., González Delgado, R. M., & Martins, L. P. 2014, *MNRAS*, 442, 1354. <https://doi.org/10.1093/mnras/stu936>
- Strömgren, B. 1937, *AJ*, 44, 216. <https://doi.org/10.1086/105501>

Herbig, G. H., & Dahm, S. E. 2002, *AJ*, 123, 1238. <https://doi.org/10.1086/338866>